

# A MOMENTUM COUPLING METHOD FOR THE UNSTEADY INCOMPRESSIBLE NAVIER–STOKES EQUATIONS ON THE STAGGERED GRID

BYOUNG-KWANG MIN AND KEUN-SHIK CHANG\*

*Department of Aerospace Engineering, Korea Advanced Institute of Science and Technology, 373-1 Kusong-dong, Yuseong-Ku, Taejeon 305-701, Republic of Korea*

## SUMMARY

A new numerical method is developed to efficiently solve the unsteady incompressible Navier–Stokes equations with second-order accuracy in time and space. In contrast to the SIMPLE algorithms, the present formulation directly solves the discrete  $x$ - and  $y$ -momentum equations in a coupled form. It is found that the present implicit formulation retrieves some cross convection terms overlooked by the conventional iterative methods, which contribute to accuracy and fast convergence. The finite volume method is applied on the fully staggered grid to solve the vector-form momentum equations. The preconditioned conjugate gradient squared method (PCGS) has proved very efficient in solving the associate linearized large, sparse block-matrix system. Comparison with the SIMPLE algorithm has indicated that the present momentum coupling method is fast and robust in solving unsteady as well as steady viscous flow problems. © 1998 John Wiley & Sons, Ltd.

KEY WORDS: incompressible Navier–Stokes flow; momentum coupling method; staggered grid; PCGS algorithm

## 1. INTRODUCTION

Good progress has been made regarding development of time-accurate numerical methods for the incompressible Navier–Stokes equations [1–6]. These methods share the difficulty of being less compact than the compressible flow formulations because the governing equations lack an explicit pressure equation. The absence of the time derivative term in the continuity equation presents another difficulty, that of disapproving the matrix form, which is powerful in the compressible flow computation.

The numerical formulations for the unsteady incompressible Navier–Stokes equations using Poisson's pressure equation can be classified into three categories. The first is the semi-implicit schemes using the uncoupled momentum equations, adopting implicit finite difference approximations for the pressure gradient terms only. The MAC method [1] is an example of this and it suffers from serious stability limitations. The second category solves the momentum equations iteratively using the implicit finite difference equations. In this case, the momentum equations are not fully coupled until a complete convergence is reached at each time level. Methods such as those from Gosman and Watkins [2] and Patanka [3] fall in this group and

\* Correspondence to: Department of Aerospace Engineering, Korea Advanced Institute of Science and Technology, 373-1 Kusong-dong, Yuseong-Ku, Taejeon 305-701, Republic of Korea. Tel.: + 82 42 8693711; fax: + 82 42 8693710; e-mail: kschang@aero5.kaist.ac.kr

are computationally heavy, since the steady iterative methods are employed at each time step to compute the unsteady flow. The methods in the third category eliminate shortcomings of the second group, as in Issa *et al.* [4] and Braza *et al.* [5]. These methods are non-iterative, but are still in the category using uncoupled momentum equations.

Apart from these earlier methods, a numerical method recently appeared adopting an approximate factorization [6]. Although it solves two momentum equations in a coupled form on the non-staggered grid, it faces the difficulty of boundary conditions on the wall in the alternative-direction sweeping process. It also had to introduce an artificial numerical dissipation term to suppress wiggles in the computation.

This paper develops a numerical formulation for the incompressible Navier–Stokes equations that solves the coupled  $x$ - and  $y$ -momentum equations simultaneously with second-order accuracy in time and space. The trapezoidal formula [7,8] is used for the time derivatives and a fully staggered grid is used to compute the momentum flux through the cell boundaries, to avoid the so-called checkerboard pressure field [3]. This method produces a block matrix equation in the predictor step that is solved in a few iterations by the PCGS (preconditioned conjugate gradient squared) algorithm [9,10]. In the correction step, the velocity and pressure variables are updated using an auxiliary potential function [11], by which the flow field finally becomes dilatation free. It has been found that the present implicit-coupled momentum formulation retrieves some cross convection terms, overlooked by the earlier implicit methods based on the uncoupled momentum equations. The present numerical method has been meticulously tested for both accuracy and convergence rate using some steady and unsteady flow problems.

## 2. TEMPORAL DIFFERENCING

The incompressible Navier–Stokes equations are written in the strong conservation law form in two dimensions

$$\frac{\partial \mathbf{q}}{\partial t} + \frac{\partial \mathbf{F}}{\partial x} + \frac{\partial \mathbf{G}}{\partial y} = 0 \quad (1)$$

$$\frac{\partial u}{\partial x} + \frac{\partial v}{\partial y} = 0, \quad (2)$$

where

$$\mathbf{q} = \begin{Bmatrix} u \\ v \end{Bmatrix}, \quad (3)$$

$$\mathbf{F} = \begin{Bmatrix} u^2 + p - \frac{1}{Re} \frac{\partial u}{\partial x} \\ uv - \frac{1}{Re} \frac{\partial v}{\partial x} \end{Bmatrix} \quad (4)$$

and

$$\mathbf{G} = \left\{ \begin{array}{l} uv - \frac{1}{Re} \frac{\partial u}{\partial y} \\ v^2 + p - \frac{1}{Re} \frac{\partial v}{\partial y} \end{array} \right\}. \tag{5}$$

Applying the trapezoidal time differencing to the momentum equation (1), a locally linearized system for the unknown vector  $\mathbf{q}$  is obtained,

$$\left[ \mathbf{I} + \frac{\Delta t}{2} \left\{ \frac{\partial \mathbf{A}}{\partial x} + \frac{\partial \mathbf{B}}{\partial y} \right\}^n \right] \mathbf{q}^{n+1} = \left[ \mathbf{I} + \frac{\Delta t}{2} \left\{ \frac{\partial \mathbf{A}}{\partial x} + \frac{\partial \mathbf{B}}{\partial y} \right\}^n \right] \mathbf{q}^n - \Delta t \left\{ \frac{\partial \mathbf{F}}{\partial x} + \frac{\partial \mathbf{G}}{\partial y} \right\}^n, \tag{6}$$

where  $\mathbf{I}$  is an identity matrix, and  $\mathbf{A}$  and  $\mathbf{B}$  are

$$\mathbf{A} = \begin{bmatrix} 2u^n - \frac{1}{Re} \frac{\partial}{\partial x}, 0 \\ v^n, u^n - \frac{1}{Re} \frac{\partial}{\partial x} \end{bmatrix}, \tag{7}$$

$$\mathbf{B} = \begin{bmatrix} v^n - \frac{1}{Re} \frac{\partial}{\partial y}, u^n \\ 0, 2v^n - \frac{1}{Re} \frac{\partial}{\partial y} \end{bmatrix}. \tag{8}$$

The vector equation (6) has the following two components

$$\begin{aligned} u^{n+1} + \frac{\Delta t}{2} \left( 2 \frac{\partial u^n u^{n+1}}{\partial x} + \frac{\partial v^n u^{n+1}}{\partial y} + \frac{\partial u^n v^{n+1}}{\partial y} - \frac{1}{Re} \nabla^2 u^{n+1} \right) \\ = u^n + \Delta t \left( - \frac{\partial p^n}{\partial x} + \frac{1}{2} \frac{1}{Re} \nabla^2 u^n \right), \end{aligned} \tag{9}$$

$$v^{n+1} + \frac{\Delta t}{2} \left( \frac{\partial u^n v^{n+1}}{\partial x} + \frac{\partial v^n u^{n+1}}{\partial x} + 2 \frac{\partial v^n v^{n+1}}{\partial y} - \frac{1}{Re} \nabla^2 v^{n+1} \right) = v^n + \Delta t \left( - \frac{\partial p^n}{\partial y} + \frac{1}{2} \frac{1}{Re} \nabla^2 v^n \right). \tag{10}$$

These equations clearly demonstrate the coupling of the  $u$ - and  $v$ -velocity components and are in the strong conservation law form, as indicated by Equation (1). Equations (9) and (10) can be represented in a unified form,

$$\begin{aligned} \frac{\varphi^{n+1} - \varphi^n}{\Delta t} + \frac{1}{2} \left( \text{div}(\varphi^n \mathbf{V}^{n+1}) + \text{div}(\varphi^{n+1} \mathbf{V}^n) - \frac{1}{Re} \text{div}(\nabla \varphi^{n+1}) \right) \\ = - \nabla p^n + \frac{1}{2} \frac{1}{Re} \text{div}(\nabla \varphi^n), \end{aligned} \tag{11}$$

where  $\mathbf{V}$  indicates the strength of the convective flow and  $\varphi$  does a transportable property of the fluid. In Equation (11),  $\varphi$  at the time level  $n$  is multiplied to the unknown vector  $\mathbf{V}^{n+1}$ , and  $\varphi$  at the time level  $n + 1$  to the vector  $\mathbf{V}^n$ . The presence of these terms distinguishes the present method from the earlier formulations reported in References [1–5].

### 3. FINITE VOLUME APPROXIMATION

The momentum equation (11) in the strong conservation law form is now integrated over control volumes: the  $u$ -cell and  $v$ -cell defined on a staggered mesh in Figure 1

$$\begin{aligned} & \iint_{A_\varphi} \varphi^{n+1} dA_\varphi + \frac{\Delta t}{2} \iint_{A_\varphi} \left( \operatorname{div}(\varphi^n \mathbf{V}^{n+1}) + \operatorname{div}(\varphi^{n+1} \mathbf{V}^n) - \frac{1}{Re} \operatorname{div}(\nabla \varphi^{n+1}) \right) dA_\varphi \\ &= \iint_{A_\varphi} \varphi^n dA_\varphi - \Delta t \iint_{A_\varphi} \nabla p^n dA_\varphi + \frac{\Delta t}{2} \frac{1}{Re} \iint_{A_\varphi} \operatorname{div}(\nabla \varphi^n) dA_\varphi. \end{aligned} \tag{12}$$

The boundary integrals occur by the Gauss divergence theorem, as in

$$\begin{aligned} & \iint_{A_\varphi} \varphi^{n+1} dA_\varphi + \frac{\Delta t}{2} \oint \left( \varphi^n \mathbf{V}^{n+1} + \varphi^{n+1} \mathbf{V}^n - \frac{1}{Re} \nabla \varphi^{n+1} \right) \cdot \mathbf{n} dl \\ &= \iint_{A_\varphi} \varphi^n dA_\varphi - \Delta t \iint_{A_\varphi} \nabla p^n dA_\varphi + \frac{\Delta t}{2} \frac{1}{Re} \oint \nabla \varphi^n \cdot \mathbf{n} dl, \end{aligned} \tag{13}$$

where  $\mathbf{n}$  is the outward unit vector normal to the boundary. Assuming that the variables  $\mathbf{V}$  and  $\nabla p$  are constant over a cell area  $A_\varphi$ , and substituting  $u$  in lieu of  $\varphi$  for the  $x$ -momentum equation, we obtain

$$\begin{aligned} & u^{n+1} A_u + \frac{\Delta t}{2} (2\Delta y (u_e^n u_e^{n+1} - u_w^n u_w^{n+1}) + \Delta x (v_n^n u_n^{n+1} - v_s^n u_s^{n+1}) + \Delta x (u_n^n v_n^{n+1} - u_s^n v_s^{n+1})) \\ & - \frac{\Delta t}{2} \left( \frac{\Delta y}{Re} \left( \frac{\partial u}{\partial x} \Big|_e - \frac{\partial u}{\partial x} \Big|_w \right)^{n+1} + \frac{\Delta x}{Re} \left( \frac{\partial u}{\partial y} \Big|_n - \frac{\partial u}{\partial y} \Big|_s \right)^{n+1} \right) = -\Delta t \frac{\partial p}{\partial x} A_u + S_u. \end{aligned} \tag{14}$$

The intermediate velocity at the cell boundary points (e, w, n and s) in Figure 1 is calculated from the nodal points (E, W, N and S) using the second-order linear interpolation. Central differencing of the spatial derivatives in Equation (14) gives, for a cell,

$$(C_u + a_p) u_p^{n+1} = \sum a_{nb} u_{nb}^{n+1} + \sum b_{nb} v_{nb}^{n+1} + \delta_x p^n + S_u, \tag{15}$$

where  $u_p$  is the value at the cell center, and the subscript  $nb$  is used to indicate neighborhood points around the  $u$ -cell. Discretization of the  $y$ -momentum equation can be made in a similar manner. The second term on the right-hand side of Equation (15), what is called ‘the cross convection term’, is brought about by coupling of the momentum equations, which do not appear explicitly in all other implicit iterative methods based on the uncoupled momentum equations. These terms contribute to improved accuracy and fast convergence for the present algorithm.

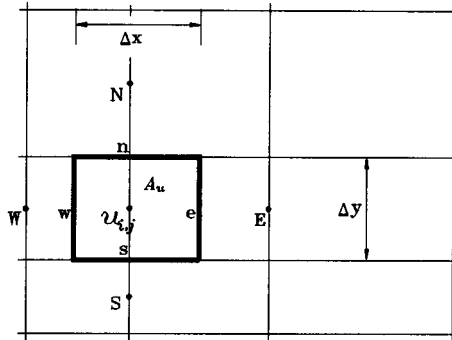
The two momentum equations, locally linear, are now represented in a matrix form in the computational domain,

$$\mathbf{C}\mathbf{X} = \mathbf{R}, \tag{16}$$

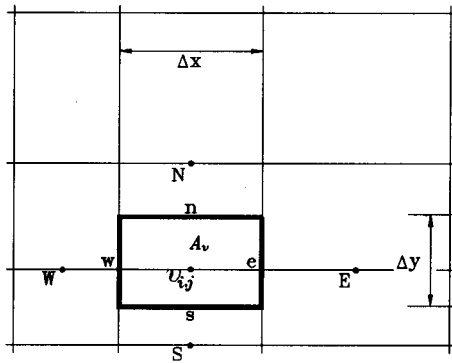
where the coefficient matrix  $\mathbf{C}$  has the following directional elements

$$\mathbf{C} = [a_{s_i,j}, a_{se_i,j}, \dots, a_{w_i,j}, a_{p_i,j}, a_{e_i,j}, \dots, a_{nw_i,j}, a_{n_i,j}]. \tag{17}$$

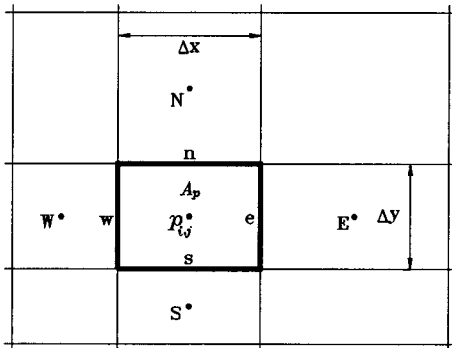
Due to the fully structured and staggered grid, the matrix  $\mathbf{C}$  becomes a banded matrix with seven block diagonals, each block being a  $2 \times 2$  matrix representing linkage between the  $u$ - and  $v$ -variables at each mesh point. In particular, when a uniform grid is used, the diagonal term



(a) u-cell



(b) v-cell



(c) p-cell

Figure 1. Staggered grid used for control volumes.

in a row of the matrix  $\mathbf{C}$  is proportional to  $\Delta x^2$  and  $\Delta t/Re$ , whereas the off-diagonal terms are proportional to  $\Delta t \Delta x$  and  $\Delta t/Re$ . The matrix  $\mathbf{C}$  then becomes less diagonally dominant when a large time step is taken for a fine mesh, or when the Reynolds number becomes large.

The solution of the linear system (16) is not divergence-free yet. Let  $\mathbf{V}^*$  be the velocity that satisfies both the continuity equation and the discretized momentum equations. Then Equation (15) can be written as

$$(C_u + a_p)u_p^* = \sum a_{nb}u_{nb}^* + \sum b_{nb}v_{nb}^* + \delta_x p^* + S_u, \quad (18)$$

where  $p^*$  is the consistent pressure that satisfies the momentum equations. Then  $\mathbf{V}^*$  and  $\mathbf{V}^{n+1}$  can be connected by an auxiliary potential function [11], namely,

$$\mathbf{V}^* = \mathbf{V}^{n+1} - \nabla \phi. \quad (19)$$

By taking a divergence in the above, a Poisson equation is obtained

$$\nabla^2 \phi = \nabla \cdot \mathbf{V}^{n+1}. \quad (20)$$

This equation is integrated over the  $p$ -cell shown in Figure 1.

The linear system of Equation (16) is solved by the matrix solver PCGS algorithm, while  $\phi$  is obtained from (20). The pressure is obtained from

$$p^* = p^n + \frac{\phi}{\Delta t}. \quad (21)$$

The velocity is calculated from Equation (19). Equation (21) is derived by substituting Equation (19), after subtracting Equation (18) from (15). The velocity field obtained this way becomes strictly divergence-free at each time level.

#### 4. PCGS METHOD

The sparse matrix  $\mathbf{C}$  in Equation (16) is asymmetric and indefinite, having elements of a  $2 \times 2$  matrix. For a high Reynolds number and a large time step, matrix  $\mathbf{C}$  may not be block diagonally dominant, since the central finite difference approximation is used to achieve second-order accuracy spacewise, as well as to reduce the numerical diffusion [12]. Many traditional iterative methods will then become unstable due to lack of diagonal dominance. The CGS algorithm [9,10] is an iterative method that achieves fast convergence in this case as long as a preconditioning matrix is properly chosen. It takes the form

$$\begin{aligned} \alpha_k &= \frac{(\mathbf{r}_0, \mathbf{r}_k)}{(\mathbf{r}_0, \mathbf{C}\mathbf{q}_k)} \\ \mathbf{h}_k &= \mathbf{p}_k - \alpha_k \mathbf{C}\mathbf{q}_k \\ \mathbf{x}_{k+1} &= \mathbf{x}_k + \alpha_k (\mathbf{p}_k + \mathbf{h}_k) \\ \mathbf{r}_{k+1} &= \mathbf{r}_k - \alpha_k \mathbf{C}(\mathbf{p}_k + \mathbf{h}_k) \\ \beta_{k+1} &= \frac{(\mathbf{r}_0, \mathbf{r}_{k+1})}{(\mathbf{r}_0, \mathbf{q}_k)} \\ \mathbf{p}_{k+1} &= \mathbf{r}_{k+1} + \beta_{k+1} \mathbf{h}_k \\ \mathbf{q}_{k+1} &= \mathbf{p}_{k+1} + \beta_{k+1} (\beta_{k+1} \mathbf{q}_k + \mathbf{h}_k). \end{aligned} \quad (22)$$

Table I. The effect of CFL number on iteration

CFL number	1.25	2.5	5.0	10.0	15.0
Average iteration number	1	1.462	2.48	7.258	11.901

Incomplete decomposition of matrix **C** into **L** and **U** as a preconditioning matrix is chosen. The sparsity patterns in **L** and **U** are given by

$$\mathbf{L} = [b_{i,j}, c_{i,j}, \dots, d_{i,j}, e_{i,j}, \dots] \tag{23}$$

and

$$\mathbf{U} = [\dots, 1, f_{i,j}, \dots, g_{i,j}, h_{i,j}]. \tag{24}$$

The elements of **L** and **U** are calculated by the method given in Reference [13].

The above algorithm was tested on a driven square cavity flow at  $Re = 1000$ , in which the Reynolds number is based on the lid velocity and the cavity dimension. Table I presents the characteristics of the linear system (16), given in terms of iteration number versus CFL number, when the residual is set by  $r \leq 10^{-6}$  in Equation (22). The iteration number in Table I represents the averaged value necessary for convergence per time step. As the increase of the CFL number makes the matrix **C** less diagonally dominant, it results in the non-linear increase of the iteration number in Table I for a fixed-convergence criterion. However, the present momentum-coupling method has shown a convergence rate faster than the SIMPLE algorithm [3] as shown in Figure 2; on the condition that the relaxation factor  $\beta$  for the steady version of SIMPLE and the time step  $\Delta t$  for the present method are to be taken as large as possible.

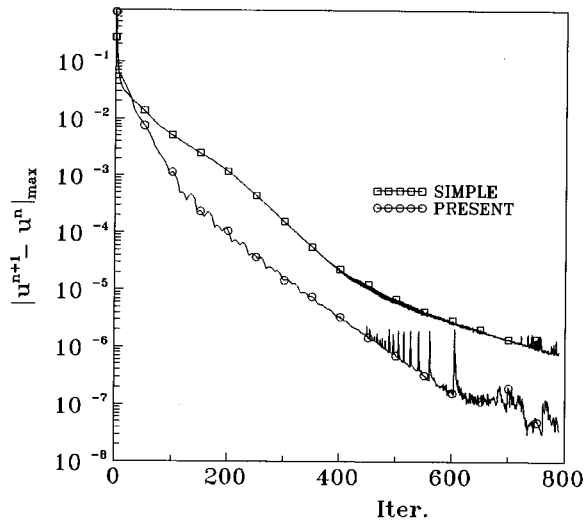


Figure 2. Convergence rate.

5. ACCURACY

The accuracy of the present method is now tested on a problem which has an exact solution. A two-dimensional unsteady flow called the Taylor problem [14] has an exact solution to the Navier–Stokes and continuity equations as

$$\left. \begin{aligned} u &= -\cos(x) \sin(y) \exp(-2t/Re) \\ v &= \sin(x) \cos(y) \exp(-2t/Re) \\ p &= -0.25(\cos(2x) + \sin(2y)) \exp(-4t/Re) \end{aligned} \right\} \quad (25)$$

For a square-flow domain  $(\pi/2, \pi/2)$ , when the exact solution is used as initial and boundary conditions, the computational residuals defined below are plotted in Figure 3(a)–(c) as a function of step sizes,  $\Delta t$  and  $\Delta x$ , and Reynolds number. The three residuals are defined by

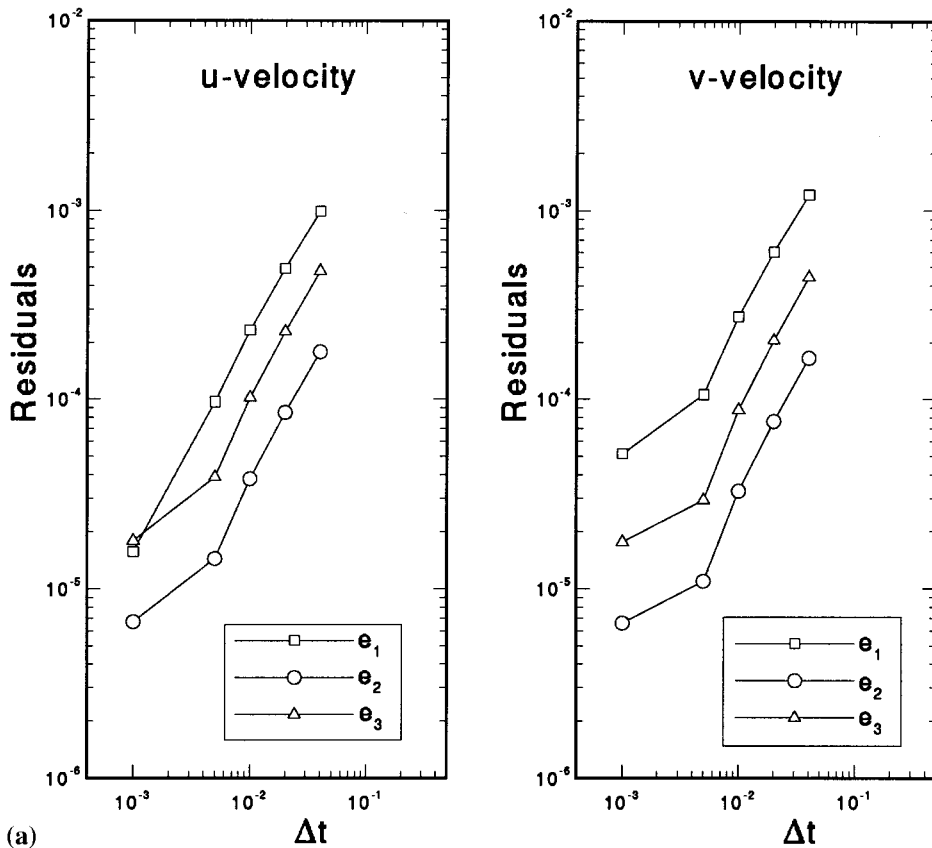


Figure 3. (a) Taylor problem: computational error vs.  $\Delta t$  ( $\Delta x = \Delta y = 0.0748$ , time = 0.6,  $Re = 10$ ). (b) Computational error vs.  $\Delta x$  ( $\Delta t = 0.01$ , time = 0.44,  $Re = 60$ ). (c) Computational error vs. Reynolds number ( $\Delta t = 0.01$ , time = 0.5,  $\Delta x = \Delta y = 0.0748$ ). —, present;  $\square$ , Braza *et al.* [5].

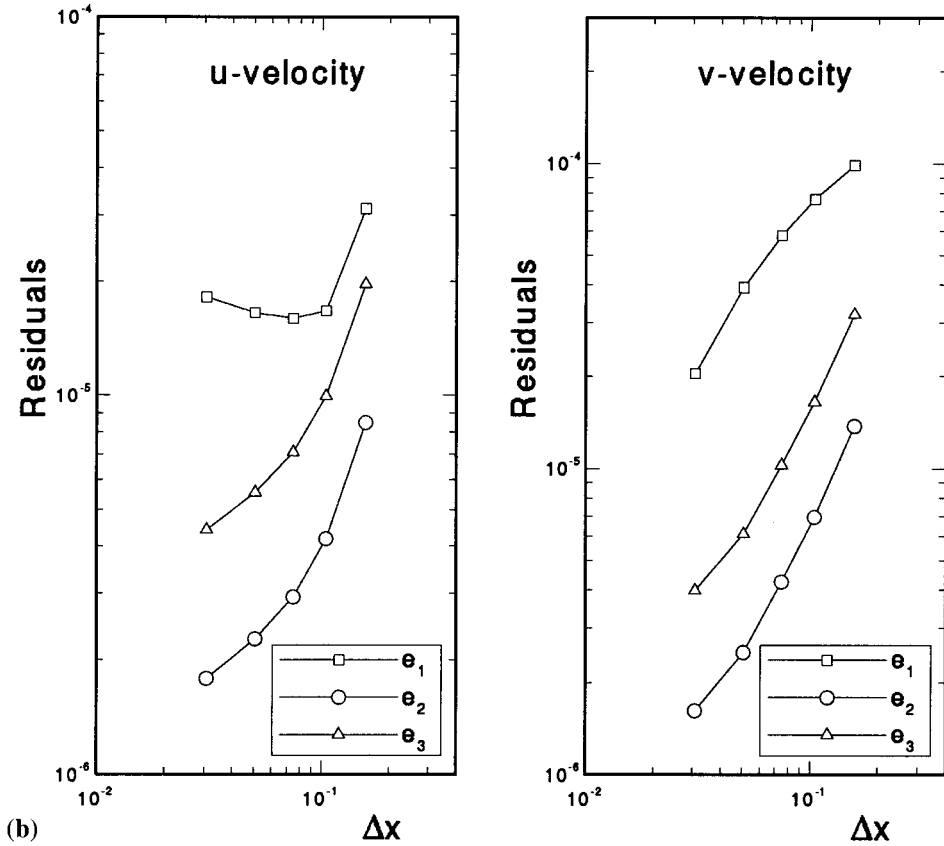


Figure 3 (Continued)

$$\left. \begin{aligned}
 e_1 &= \max(|F_{i,j} - f_{i,j}|) \\
 e_2 &= \sum (|F_{i,j} - f_{i,j}|) / N_x \times N_y \\
 e_3 &= \sum (|F_{i,j} - f_{i,j}|) / \sum |F_{i,j}|
 \end{aligned} \right\} \quad (26)$$

where  $F$  represents the analytical solution,  $f$  the numerical solution and  $N_x$  and  $N_y$  the number of nodes in the computational domain.

When the time step and mesh sizes are decreased, the logarithmic residual norm decreases linearly. This indicates that the present method is of second-order accuracy in time and space. Exact solutions in Equation (25) suggest that increasing the Reynolds number results in the slow variation of the variables with time. This implies that the numerical solution will give good agreement with the analytical solution as the Reynolds number is raised. Figure 3(c) clearly shows this, demonstrating the superiority of the present method over Reference [5]. The residuals monotonically decrease with the Reynolds number to the lowest value,  $10^{-6}$ , which is a very desirable feature in contrast to Reference [5].

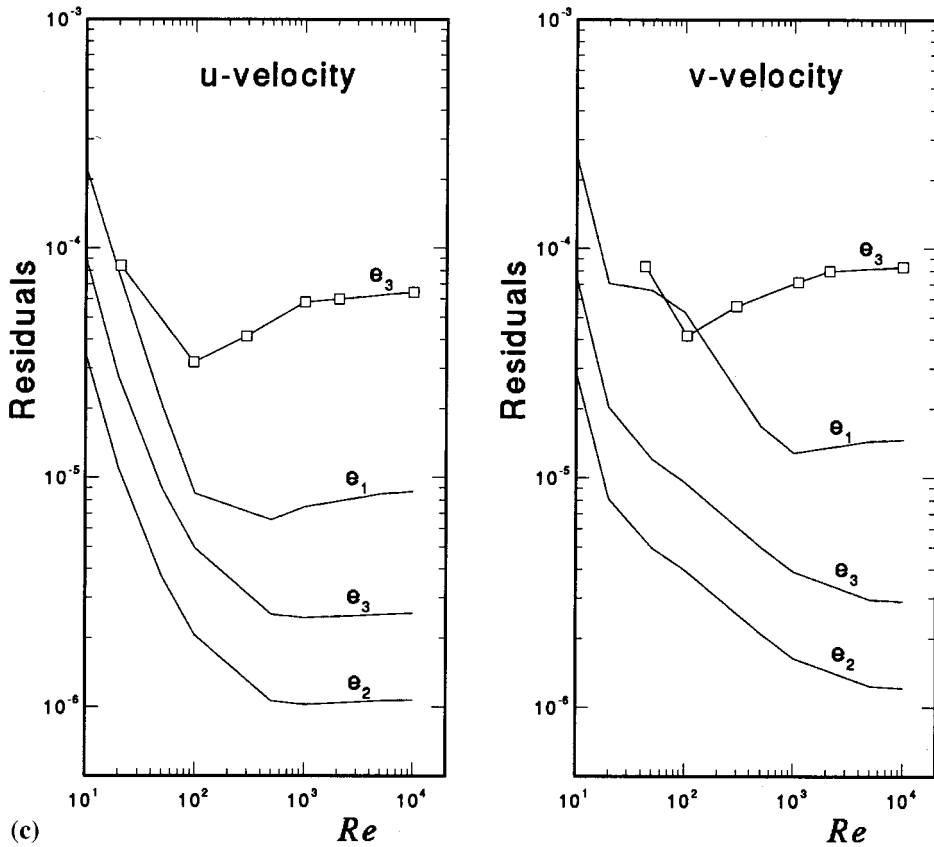


Figure 3 (Continued)

Figure 4 compares the CPU time, on a HP 735 workstation, used by the present method and that by the steady state version of the SIMPLE algorithm, to get the steady state solution for a driven square cavity flow. The mesh is a uniform  $25 \times 25$ , and the Reynolds number, based on the lid velocity,  $V$ , and the wall length, is 400. It is well-known that iterative methods require an underrelaxation factor,  $\beta$ , for convergence due to the convection terms. However, there is no general rule for the optimum value of  $\beta$ . It depends on many factors such as the nature of flow, the number of grid points, the time step size and the specific iterative procedure. As shown in Figure 4, the performance of SIMPLE is very sensitive to the relaxation factor  $\beta$ ; the scheme, in fact, diverges beyond the value  $\beta = 0.52$ . In contrast, the curve obtained by the present method is quite flat over a wide range of CFL numbers, demonstrating the stability and robustness of the numerical method. Of course, the particular SIMPLE algorithm used in the present comparison may not be the one tuned to produce the best results, but it strongly indicates the healthy characteristics of the present numerical method.

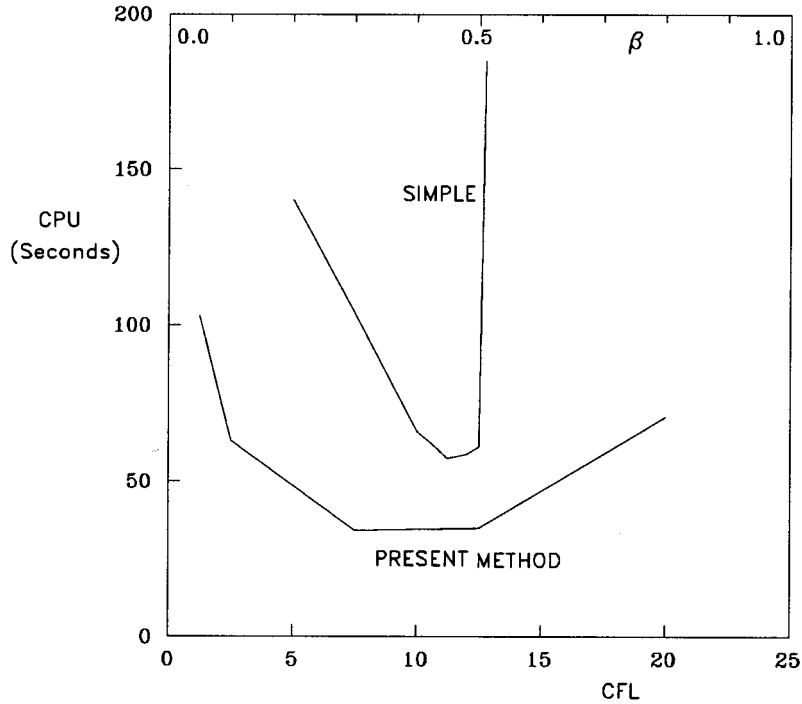


Figure 4. The square-driven cavity flow: comparison of CPU time.

## 6. TEST PROBLEMS

### 6.1. Steady-driven cavity flow

The present method is compared with that of Ghia *et al.* [15] in Figure 5, in which the  $u$ -velocity profile is plotted for different Reynolds numbers along the central vertical line of the square cavity. The abscissa of the curve for each increasing Reynolds number is shifted sequentially by  $-0.2$  from that of  $Re = 100$ , for the clarity of presentation. Here, the

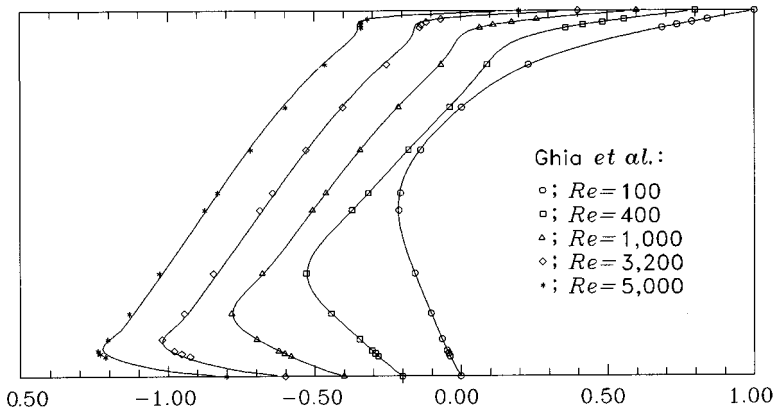


Figure 5. Square cavity flow:  $u$ -velocity profile along the vertical centerline. Solid line represents present results.

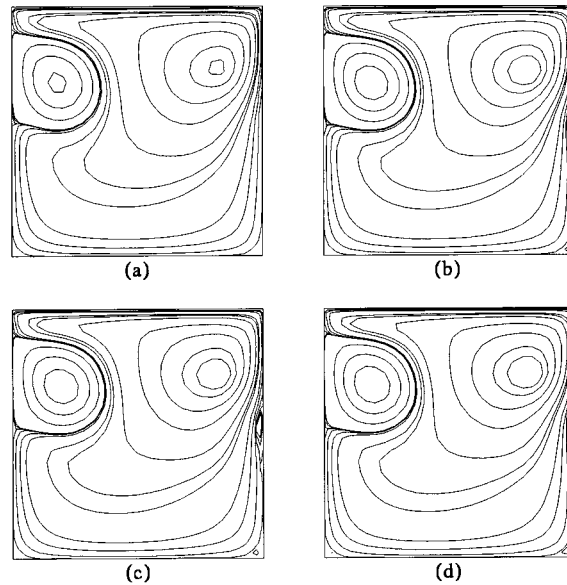


Figure 6. Streamlines in driven cavity flow (time =  $\pi/2$ ,  $Re = 1000$ ). (a) SIMPLE with no subiterations, (b) SIMPLE after 10 subiterations, (c) SIMPLE after 50 subiterations, (d) present computation.

numerical results are obtained up to  $Re = 5000$  with the stretched grid  $70 \times 70$ ; high Reynolds number flow ( $Re > 3000$ ) exhibits kinks in the curve near the wall, which agrees well with the results given by Ghia *et al.*

### 6.2. Flow in a cavity with an oscillating wall

Computed as a second test is a square-driven cavity flow by the top wall, oscillating with  $u = \cos(t)$ . Here, the non-dimensional variables are

$$u = u^*/U_0, \quad x = x^*/a, \quad y = y^*/a, \quad t = \omega t^*, \quad (27)$$

where  $U_0$  is the maximum velocity of the oscillating wall,  $a$  is the wall length and  $\omega$  is the frequency. Two non-dimensional parameters are possible: the Reynolds number,  $Re = U_0 a/\nu$ , and the frequency parameter,  $\beta = \omega a^2/\nu$ .

The flow aspect inside a cavity depends on the two parameters,  $Re$  and  $\beta$  (see Reference [16]);  $Re = \beta$  is chosen here to construct a meaningful flow in which the non-linear terms in the Navier–Stokes equations cause maximum effect. In other words, deliberately excluded are the extreme, well-known cases like the Stokes' second problem, the boundary layer flow and the less interesting quasi-steady flow. Figure 6 depicts the selected streamlines at time  $t = \pi/2$ , when the upper wall is momentarily at a dead point after the first half period. The fluid motion is then a measure of the time lag, as indicated in Reference [16]. The time step  $\Delta t$  was 0.04 and the mesh was  $30 \times 30$ , with the smallest grid spacing,  $\Delta x = \Delta y = 0.0125$ ; the grid is clustered near the walls to resolve the boundary layer. Figure 6(a)–(c) represent the results of the iterative version of SIMPLE: Figure 6(a) obtained without any subiterations, Figure 6(b) after 10 subiterations and Figure 6(c) after 50 subiterations. In contrast, Figure 6(d) is obtained by the present method. Comparison indicates that the secondary vortex bubble in the middle of the right wall is not correctly captured by the SIMPLE method until the subiterations become

as many as 50. The CPU time to get the solution in Figure 6(d) was 140 s on a HP 735 workstation, while that for Figure 6(c) was 2752 s.

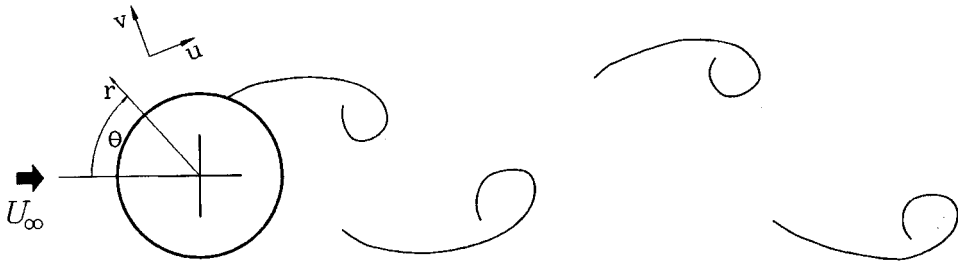
6.3. Flow around a circular cylinder

Finally, the unsteady flow related to instability of the shear layer was investigated. Figure 7 shows both the sketch of a circular cylinder and the artificial perturbation used in the computation to expedite the quasi-steady vortex shedding. A modified polar co-ordinate system is used here to embed a mesh finer toward the cylinder surface, as

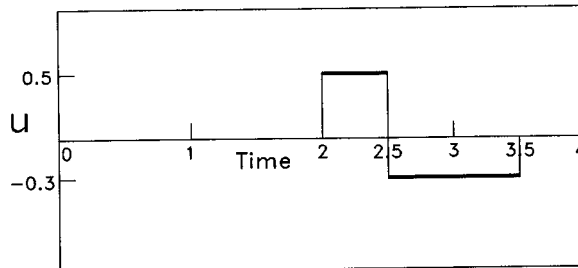
$$\begin{aligned} x &= \theta, & u &= V_\theta, \\ y &= \log r, & v &= V_r. \end{aligned}$$

The flow variables are scaled by the free stream velocity  $U_\infty$ , the radius of the cylinder  $a$  and the dynamic pressure  $\rho U_\infty^2$ . The no-slip boundary condition was applied on the cylinder surface, and the Oseen solution [18] on the far boundary in the form

$$\mathbf{V}(x, y)_{y=y_\infty} \rightarrow U_\infty, \quad \text{outside the wake region,} \tag{28}$$



(a)



(b)

Figure 7. Vortex shedding behind a circular cylinder (a), with the time-dependent numerical perturbation (b).

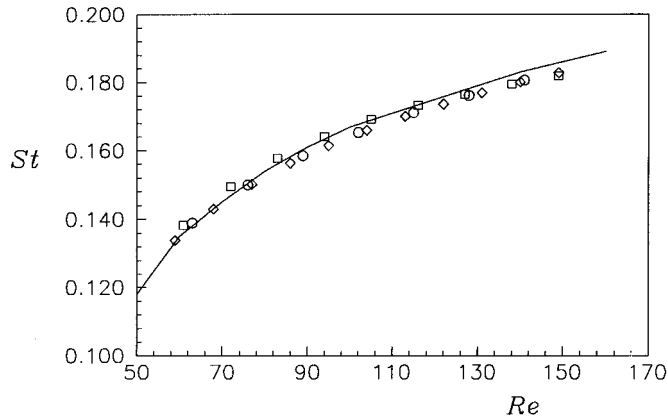


Figure 8. Strouhal numbers vs. Reynolds numbers. —, present results; □, Roshko [23], ○, Williamson [24], ◇, Norberg [25].

$$\left. \frac{\partial \mathbf{V}(x, y)}{\partial y} \right|_{y=y_\infty} \rightarrow 0, \quad \text{in the wake region.} \quad (29)$$

The computed velocity field does not, in general, satisfy the global mass conservation. Namely,

$$\int_0^{2\pi} v(x, y_\infty) dx \neq 0. \quad (30)$$

This implies that we cannot keep the compatibility condition by a Neumann condition used at the exit for the Poisson equation (20), ending up with a non-convergent iterative solution [17]. To ensure the overall mass conservation, the mass flow rate at the outlet boundary condition is corrected by evenly distributing the mass residual, calculated from Equation (30), to the  $u$ -cells satisfying Equation (29). Updating of velocity and pressure is then made in the correction step in the manner already shown in Section 3.

The Strouhal number is plotted in Figure 8 as a function of Reynolds number, for  $Re \leq 150$ . A good agreement with the experimental results is clear. The present data are obtained with the grid  $60 \times 80$ ,  $\Delta t = 0.05$  and the far boundary at  $R_\infty = 115$ . Figure 9 shows the instantaneous streamlines during half a period for a high Reynolds number,  $Re = 1000$ . The initial time  $t = 0$  corresponds to the instant of maximum drag coefficient, and the half period time  $t = T/2$  to that of minimum drag coefficient. The distinct feature here is that the secondary vortices are adhered to the rear of the cylinder. These secondary vortices periodically merge with one another and also with the primary eddy in the Kármán vortex street. The merging of the vortices described by Braza *et al.* [5] is clear here. Figure 9(a) and (b) show that a small eddy in the upper side merges with the dominant central eddy. Figure 9(c) and (d) show that two eddies rotating in the same direction in the lower side of the rear of the cylinder are merged into one. Figure 9(e)–(h) show that two secondary eddies of about equal size merge into one having greater eddy strength. Such merging results in a bigger eddy which is swept away into the main wake region. The present results evidently show the pattern of the near wake formation in more detail than any other report.

The particles injected from the cylinder are swept into the vortices. They present an idea where the vorticity is distributed in the flow field. Bearman and Graham [19] have indicated that while the Strouhal number and the drag coefficient could be well predicted by computa-

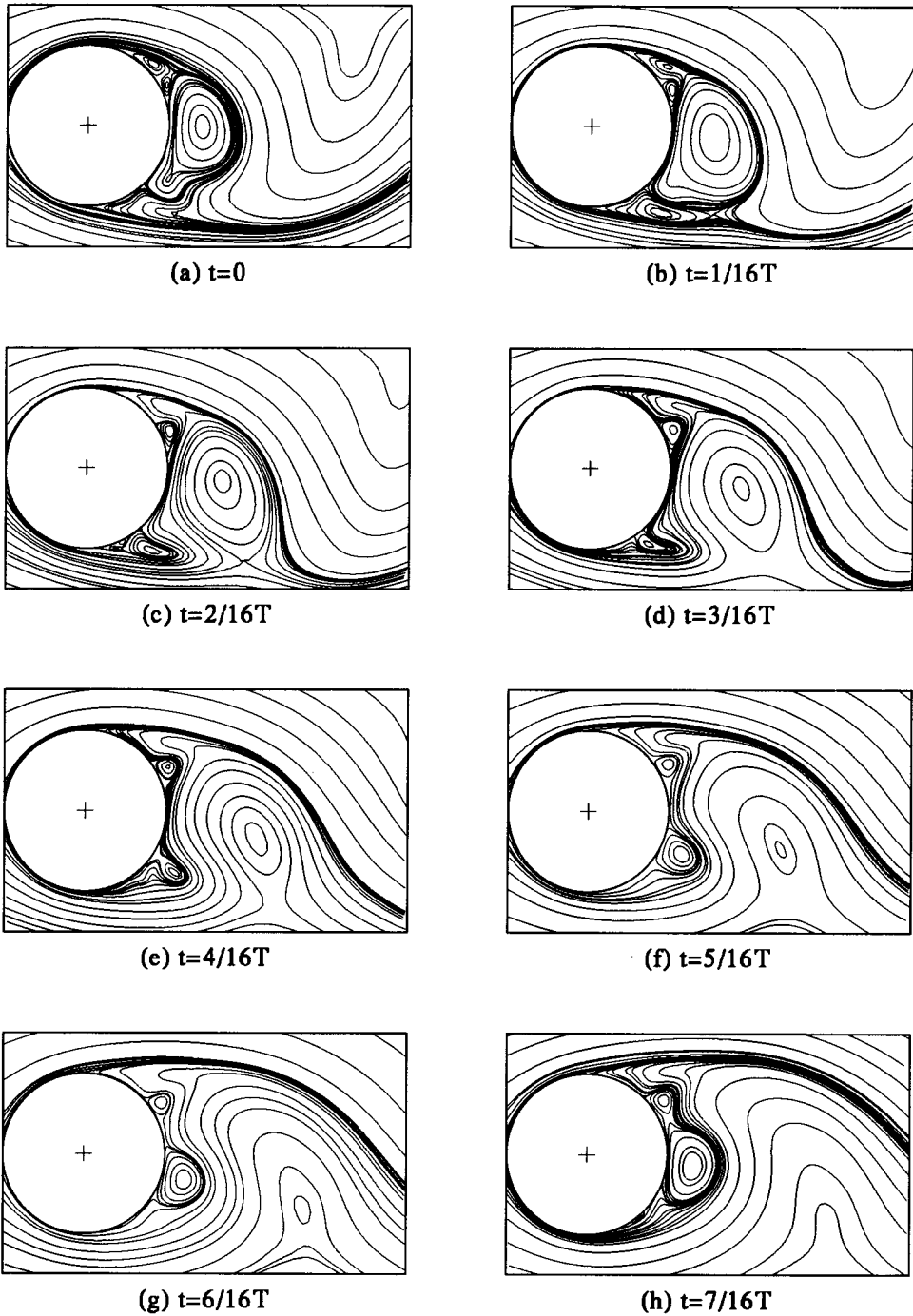
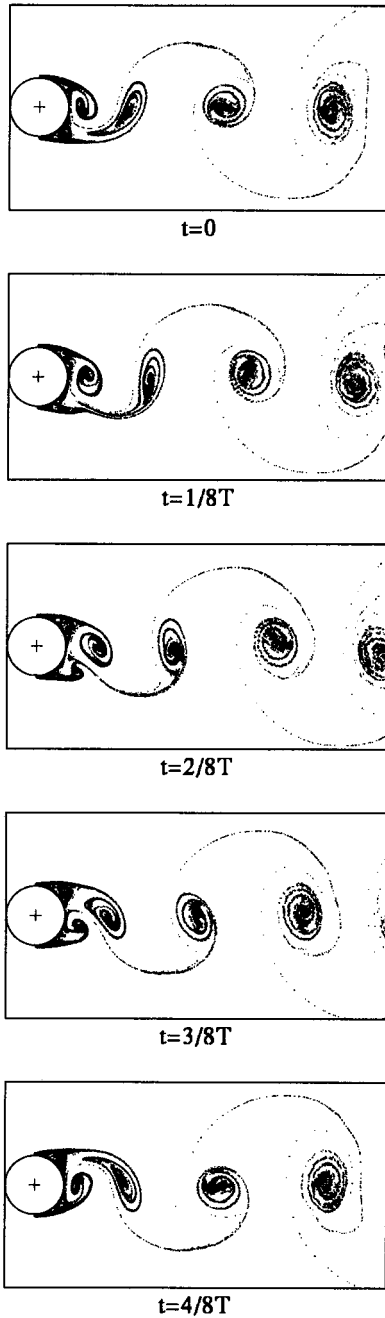


Figure 9. Streamlines for half a period at  $Re = 1000$ .

Figure 10. Streaklines at  $Re = 1000$ .

tion, details of the vortex-shedding pattern revealed by the computed streamlines and streaklines could be different from the experiment. When too coarse a grid is used, along with non-bounded difference schemes such as central difference and the Leonard QUICK scheme [20], to compute a flow field of large gradient, it is well known that wiggles can be brought about in the computation.

For a high Reynolds number flow, the region of large flow gradient is extended further in the wake; hence a coarse grid cannot properly handle the flow. Our numerical experiment showed, however, that reducing the far boundary in the present circular computational domain did not sensibly influence the basic flow pattern except that only the Strouhal number and the force coefficients are changed a little. Chosen as a test was a narrow far boundary at  $R_\infty = 30$  with a grid size  $180 \times 160$  in order to obtain the vortex pattern at  $Re = 1000$ , which is a severe computational condition. Each frame of Figure 10 shows streaklines for  $Re = 1000$ , which were obtained through ten particle injection ports from each of which a new particle is injected at time interval  $\Delta t = 0.02$ . Tritton [21] and Gerrard [22] have indicated that vortex shedding is in the direct shedding mode beyond the transition Reynolds number,  $Re = 80$ . In Figure 10, it is observed that the vortex near the cylinder is first indented and then folded up to grow as a vortex core in a process similar to the roll-up of a vortex sheet. The vortex street here is clearly developed by the direct shedding without any hint of wake instability. The vortices are stretched and elongated, taking circular shapes as they move into the far wake region. The time-dependent drag and lift coefficients plotted in Figure 11 show strict periodicity. Obtained was a Strouhal number of 0.22, with the far boundary at  $R_\infty = 115$ ; in contrast to the Strouhal number of 0.24 obtained with the far boundary at  $R_\infty = 30$ . It is compared with the value 0.21 given by Braza *et al.* [5] The frequency of drag coefficient is naturally twice that of the lift coefficient.

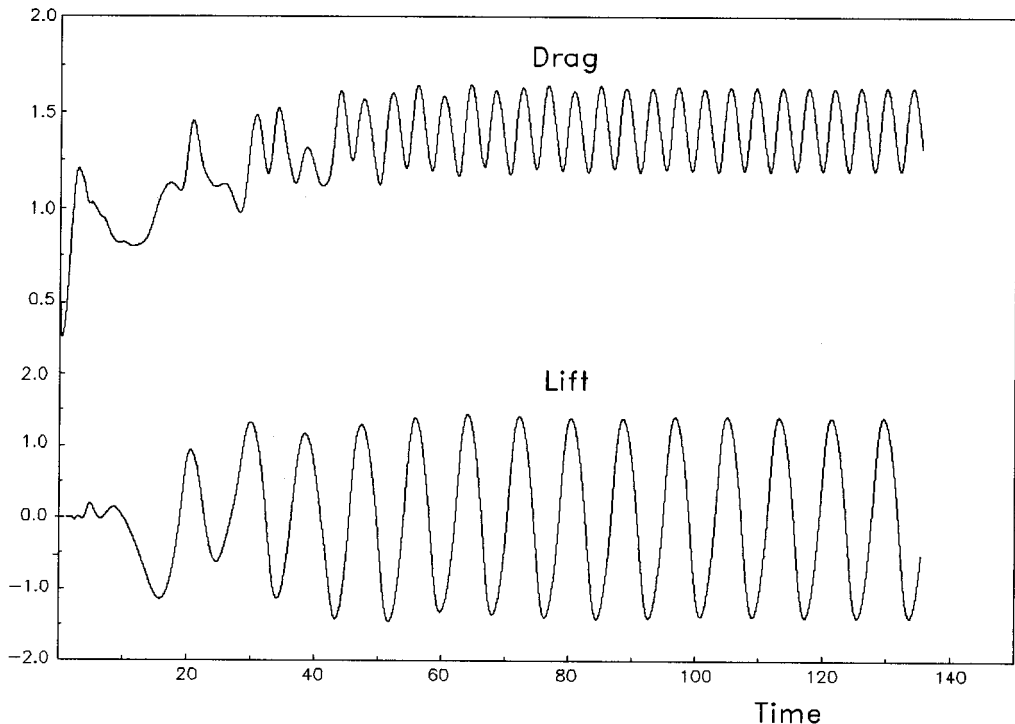


Figure 11. Time evolution of the force coefficients at  $Re = 1000$ .

## 7. CONCLUSION

In this paper, a new solution method called the ‘*momentum-coupling method*’ is formulated to solve the unsteady incompressible Navier–Stokes equations. This method maintains second-order accuracy in space and time. The present method shows fast convergence and good stability properties in a relatively large parameter range. The method does not anticipate any hindrance in extending the present two-dimensional formulation to three dimensions, except that a more full-frame computer facility is required. The algorithm has demonstrated fast convergence, robustness and accuracy in computing several benchmark problems such as the Taylor problem, the square-driven cavity flow and the cavity with an oscillating wall. In addition, tests on a flow past a circular cylinder proved that a high Reynolds number flow, e.g.  $Re = 1000$ , can be computed without difficulty and a very detailed flow pattern associated with direct vortex shedding can be observed.

## REFERENCES

1. F.H. Harlow and J.E. Welch, ‘Numerical calculation of time-dependent viscous incompressible flow of fluid with free surface’, *Phys. Fluids*, **8**, 2182–2189 (1965).
2. A.D. Gosman and A.P. Watkins, in *Proc. 1st Symp. on Turbulent Shear Flows*, Pennsylvania State University, 1977.
3. S.V. Patanka, *Numerical Heat Transfer and Fluid Flow*, McGraw-Hill, New York, 1980.
4. R.I. Issa, A.D. Gosman and A.P. Watkins, ‘The computation of compressible and incompressible recirculating flows by a non-iterative implicit scheme’, *J. Comput. Phys.*, **62**, 66–82 (1986).
5. M. Braza, P. Chassaing and H. Ha Minh, ‘Numerical study and physical analysis of the pressure and velocity fields in the near wake of a circular cylinder’, *J. Fluid Mech.*, **165**, 79–130 (1986).
6. M.L. Mansour and A. Hamed, ‘Implicit solution of the incompressible Navier–Stokes equations on a non-staggered grid’, *J. Comput. Phys.*, **86**, 147–167 (1990).
7. W.E. Milne, *Numerical Solution of Differential Equation*, Wiley, New York, 1953.
8. G. Dahlquist and A. Björck, *Numerical Methods*, Prentice-Hall, Englewood Cliffs, NJ, 1974.
9. S. Kaushik and P.L. Hagelstein, ‘The application of the preconditioned biconjugate gradient algorithm to NLTE rate matrix equations’, *J. Comput. Phys.*, **101**, 360–367 (1992).
10. C.P. Jackson and P.C. Robinson, ‘A numerical study of various algorithms related to the preconditioned conjugate gradient method’, *Int. j. numer. methods eng.*, **21**, 1315–1338 (1985).
11. A.A. Amsden and F.H. Harlow, ‘The SMAX method: a numerical technique for calculating incompressible fluid flows’, *Los Alamos Sci. Rep. No. La-4370*, 1970.
12. J.M. Leone Jr., and Philip M. Gresho, ‘Finite element simulations of steady, two-dimensional, viscous incompressible flow over a step’, *J. Comput. Phys.*, **41**, 167–191 (1981).
13. H.L. Stone, ‘Iterative solution of implicit approximation of multidimensional partial differential equation’, *SIAM J. Numer. Anal.*, **5**, 530–558 (1968).
14. G.K. Batchelor (ed), *The Collected Works of G.I. Taylor*, vol 2, Cambridge University Press, Cambridge, 1960.
15. U. Ghia, K.N. Ghia and C.T. Shin, ‘High  $Re$  solutions for incompressible flow using the Navier–Stokes equations and a multigrid method’, *J. Comput. Phys.*, **48**, 387–411 (1982).
16. P.W. Duck, ‘Oscillatory flow inside a square cavity’, *J. Fluid Mech.*, **122**, 215–234 (1982).
17. P.J. Roache, *Computational Fluids Dynamics*, Hermosa, Albuquerque, NM, 1976.
18. S.C.R. Dennis and Gau-Zu Chang, ‘Numerical solutions for steady flow past a circular cylinder at Reynolds numbers up to 100’, *J. Fluid Mech.*, **42**, 471–489 (1970).
19. P.W. Bearman and J.M.R. Graham, ‘Vortex shedding from bluff bodies in oscillatory flow: a report on Euromech 119’, *J. Fluid Mech.*, **99**, 225–245 (1980).
20. B.P. Leonard, ‘A stable and accurate convective modeling procedure based quadratic upstream interpolation’, *Comp. Methods Appl. Mech. Eng.*, **19**, 59–98 (1979).
21. D.J. Tritton, ‘Experiments on the flow past a circular cylinder at low Reynolds numbers’, *J. Fluid Mech.*, **6**, 547–567 (1959).
22. J.H. Gerrard, ‘The Wakes of cylindrical bluff bodies at low Reynolds number’, *Philos. Trans. R. Soc. Lond. A*, **288**, 351–382 (1978).
23. A. Roshko, *On the Drag and Shedding Frequency of Two-Dimensional Bluff Bodies*, National Advisory Committee Aeronautics, TN, 1954.
24. C.H.K. Williamson, ‘Oblique and parallel modes of vortex shedding in the wake of a circular cylinder at low Reynolds numbers’, *J. Fluid Mech.*, **206**, 579–627 (1989).
25. C. Norberg, ‘An experimental investigation of the flow around a circular cylinder: influence of aspect ratio’, *J. Fluid Mech.*, **258**, 287–316 (1994).